PHYSICSAccess Research Paper
ISSN Online: 2756-3898, ISSN Print: 2714-500X https://doi.org/10.47514/phyaccess.2026.6.1.004

High-Efficiency Cs_2TiBr_6 Lead-Free Perovskite Solar Cell Enabled by All-inorganic CZTS/NiO Double Hole Transport Layer: A Numerical Simulation Study

Peverga R Jubu[1, 2, 3], Michael O Awoji[4], Bunmi J Akeredolu[4], Adebayo T Adepoju[3], Sekav J Ikwe[5], Denen S Igba[6], Francis Aungwa[3], Terdoo M Ikpa[3], Iheke M Nwachukwu[7], and Emeka E Oguzie[1, 8]

[1] Africa Centre of Excellence in Future Energies and Electrochemical Systems (ACE-FUELS), Federal University of Technology Owerri (FUTO), P.M.B. 1526 Owerri, Imo State, Nigeria.
[2] Institute of Nano-Optoelectronics Research and Technology (INOR), Universiti Sains Malaysia, 11800 USM, Penang, Malaysia.
[3] Department of Industrial Physics, Joseph Sarwuan Tarka University, Makurdi (Federal University of Agriculture Makurdi) P.M.B. 2373, Makurdi, Benue State, Nigeria.
[4] Department of Physics, Federal University Wukari, Taraba State, Nigeria.
[5] Basic and Applied Science Institute, Egypt-Japan University of Science and Technology, New Borg El-Arab 21934, Egypt.
[6] Department of Physics, Joseph Sarwuan Tarka University, Makurdi, P.M.B. 2373, Makurdi, Benue State, Nigeria.
[7] Department of Physics, National Open University of Nigeria, Abuja.
[8] Department of Chemistry, Federal University of Technology Owerri (FUTO), P.M.B. 1526 Owerri, Imo State, Nigeria.

Corresponding E-mail: peverga.jubu@uam.edu.ng

Received 06-12-2025
Accepted for publication 09-02-2026
Published 11-02-2026

Abstract

Ti-based Cs_2TiBr_6 double-halide perovskites are promising for optoelectronic and renewable energy applications, offering a non-toxic alternative to Pb-based perovskite solar cells (PSCs). This study uses SCAPS-1D to simulate a Cs_2TiBr_6-based PSC incorporating a CZTS/NiO double hole transport layer (HTL) to enhance power conversion efficiency (PCE). The double HTL improves hole transport, strengthens electron blocking, and reduces interfacial recombination. The optimized FTO/CeOx/Cs_2TiBr_6/CZTS/NiO/Au architecture achieves a PCE of 27.78%, significantly higher than the prototype (11.62%), under optimized parameters including absorber and interface defect densities, electron capture cross-section, and CZTS thickness. Notably, the ETL-free structure (FTO/Cs_2TiBr_6/CZTS/NiO/Au) attains the same PCE (27.78%), indicating that the CeOx ETL is dispensable for a simplified, and cost-effective design. The achieved efficiency exceeds previous reports on Cs_2TiBr_6-based PSCs.

Keywords: Cs_2TiBr_6 perovskite; Photovoltaic; Solar cell; CZTS and NiO; SCAPS-1D.

I. Introduction

The rapid increase in environmental degradation issues and the global energy demand necessitate the demand for clean and efficient renewable energy sources [1, 2]. Among the various options, solar energy stands as a dependable and sustainable choice, utilizing solar cell technology that directly converts sunlight into electricity [3, 4]. Although silicon-based solar cells currently lead the market owing to their established and demonstrated reliable technology, their energy-intensive and costly production, particularly for monocrystalline silicon, significantly impacts the environment, which limits large-scale commercialization [5]. PSCs offer advantages such as superior light absorption, tunable band gaps, and enhanced absorption coefficients, as well as cost-effective solution-based manufacturing under mild fabrication conditions [4, 6, 7].

Lead-free inorganic perovskite, such as calcium titanium bromide (Cs_2TiBr_6), is a double-halide absorber material whose formula fits the A_2BX_6 type (where $A = Cs, B = Ti, X = Br$). This material exhibits potential for solar cells owing to its thermal stability and eco-friendliness, in contrast to lead-based alternatives [5, 8]. Its indirect band gap of approximately 1.8 eV is suitable for solar energy applications [6]. However, their efficiencies are often limited by the lower optical absorption of lead halide perovskites. Additionally, its relatively low carrier mobility and high defect density are identified as critical challenges [8]. To overcome these drawbacks, researchers emphasize the importance of interface engineering, defect passivation, and heterostructure design to improve carrier transport and reduce recombination losses [9]. Despite its inherent challenges, the Cs_2TiBr_6 perovskite benefits from high structural stability, tolerance to temperature variations, and resistance to degradation under ambient conditions, which are significant advantages for long-term device performance [6, 8].

The limited research on Cs_2TiBr_6 perovskite exists primarily due to the challenges in selecting suitable electron transport layers (ETLs) and hole transport layers (HTLs) that can be effectively incorporated with the Cs_2TiBr_6 perovskite to achieve high solar cell efficiency [8]. Chen et al. performed the first experimental study on planar-heterojunction Cs_2TiBr_6 perovskite solar cells (PSCs) via a low-temperature vapor phase two-step synthesis route and exhibited a 3.3% PCE [7]. Reference [6] recorded a PCE of 2.34% from an HTL-free Cs_2TiBr_6 PSC prepared by the spin-coating method. Meanwhile, a handful of theoretical reports are available for this perovskite absorber; however, only a few have recorded PCE of > 20.0% [5, 8–12]. The following higher theoretical PCE values have been reported so far, using various PSC configurations: 26.96% [10], 24.24% [9], 24.82% [5], 23.77% [11], 22.61% [8], 21.17% [12], and 20.11% [13]. The $Pt/CuSbS_2/Cs_2TiBr_6/ZnO/FTO$ Solar cell architecture yielded 26.96% PCE [10], while $FTO/CeOx/Cs_2TiBr_6/CZTS/P_3HT/Au$ cell configuration displayed 22.61% [8] (where CZTS = copper zinc tin sulfide; P_3HT = poly(3-hexylthiophene)) [8].

The careful selection of materials for the cell holds potential for enhanced performance if certain layers are substituted with a more appropriate material [8]. For instance, the P_3HT HTL employed in this structure is much pricier because it needs to be synthesized organically with a high level of purity and specific structural arrangements for its use in electronics [8]. Also, its large-scale production is still limited compared to inorganic materials. NiO is an inorganic p-type wide bandgap semiconductor that can be easily synthesized from affordable raw materials via simple and scalable methods. Its production is already at the industrial scale for ceramics, catalysis, and electrodes [14]. Pertinently, NiO can serve as a better HTL compared to P_3HT because its hole mobility of $20.0\ cm^2V^{-1}\ s^{-1}$ [15] is significantly higher than that of P_3HT (2.0 $cm^2V^{-1}s^{-1}$) [8]. NiO promotes better energy band alignment with Cs_2TiBr_6/CZTS and enhances electron blocking, resulting in superior charge selectivity (more efficient hole extraction and transport) and stability in the FTO/CeO_x/Cs_2TiBr_6/CZTS/NiO/Au PSC design.

A key advancement of this study is the integration of some unique simulation parameters to achieve a simplified design framework with improved performance. Contrary to the design by [8], a lower absorber thickness of 500 nm, which is much easier to deposit, and a lower electron capture cross-section of 1×10^{-19} cm^2 to tighten Shockley-Read-Hall (SRH) recombination control, so that fewer photogenerated carriers can be lost through defect states, are used in the optimized simulation. Also, the influence of operating temperature is investigated in a wider range (300-500 K) to predict the robustness of the device. To add more uniqueness to the concept, the current work investigates the ETL-free counterpart configuration (FTO/Cs_2TiBr_6/CZTS/NiO/Au) to understand the effect of eliminating the ETL (CeO_x) from the conventional design (FTO/CeO_x/Cs_2TiBr_6/CZTS/NiO/Au ETL-free PSCs are advantageous and have received significant interest recently, due to their cost-effectiveness and simplified fabrication process [16-20]. Interestingly, experimental studies have shown that the ETL-free PSCs can achieve high PCEs. Reference [19] obtained a PCE of 13.50% with and without the use of ZnO ETL in a PSC design. Similarly, [20] recorded a PCE of 19.52% with and without integrating an ETL in a cell. Other experimental PCE values of 20.10% [18], 22.0% [16], 20.0% [17], 13.60% [21] have also been reported, validating the robustness of the ETL-free design.

This study explores the modified PSC multi-layer architecture (FTO/CeO_x/Cs_2TiBr_6/CZTS/NiO/Au) and the rarely exploited ETL-free counterpart (FTO/ Cs_2TiBr_6/CZTS/NiO/Au) using SCAPS-1D simulation. The modified designs incorporating the additional NiO HTL

broaden the absorption spectrum, reduce energy loss, and mitigate charge recombination by enhancing band alignment and boosting the charge migration mechanism. Notably, adjusting key parameters such as thickness, defect density, electron capture cross-section, interface quality, and eliminating the ETL can substantially boost PCE, thereby advancing the practical viability of Cs_2TiBr_6-based devices.

II. Numerical Modelling

The SCAPS-1D model simulates semiconductor devices by solving a set of three fundamental equations, including Poisson's equation (1), the electron continuity equation (2), and the hole continuity equation (3). By applying these coupled partial differential equations, the software determines the distribution of electrons and holes within the electrostatic potential as a function of position (x). From these solutions, SCAPS-1D evaluates key device characteristics, such as short-circuit current density (J_{SC}), quantum efficiency (QE), energy band structure, and current-voltage (J-V) behavior [10].

$$-\frac{\partial}{\partial}\left(-\varepsilon x\frac{\partial V}{\partial x}\right) = q[p(x) - n(x) + N_D^+(x) - N_A^-(x) + p_t(x) - n_t(x)] \quad (1)$$

$$\frac{\partial n}{\partial t} = \frac{1}{q}\frac{\partial J_n}{\partial x} + G_n - R_n \quad (2)$$

$$\frac{\partial p}{\partial t} = \frac{1}{q}\frac{\partial J_p}{\partial x} + G_p - R_p \quad (3)$$

Where V is the potential, q is the charge, ε is the dielectric permittivity, $p(x)$ is the free holes concentration, $n(x)$ is the free electrons concentration, $N_A^-(x)$ is the acceptor carrier density, $N_D^+(x)$ is the donor carrier density, $p_t(x)$ is the trap density of the hole, $n_t(x)$ is the trap density of electrons, J_n is the current density of electrons, J_p is the current density of holes, G_p is the holes generation rate, G_n is the electrons generation rate, R_p is the recombination rate of holes, and R_n is the recombination rate of electrons.

A. Solar Cell Architectures

Three prototype PSC structures (FTO/CeO_x/Cs_2TiBr_6/CZTS/Au, TO/CeO_x/Cs_2TiBr_6/NiO/Au, and FTO/CeO_x/Cs_2TiBr_6/CZTS/NiO/Au) were designed with Cs_2TiBr_6 as the absorber layer, and FTO and Au as the front and back contact electrodes as illustrated in Fig. 1a, with the corresponding energy band diagram depicted in Fig. 1b, respectively. To ensure comparability, the thickness, carrier concentration, and defect density of the various HTLs were kept consistent across all the three devices.

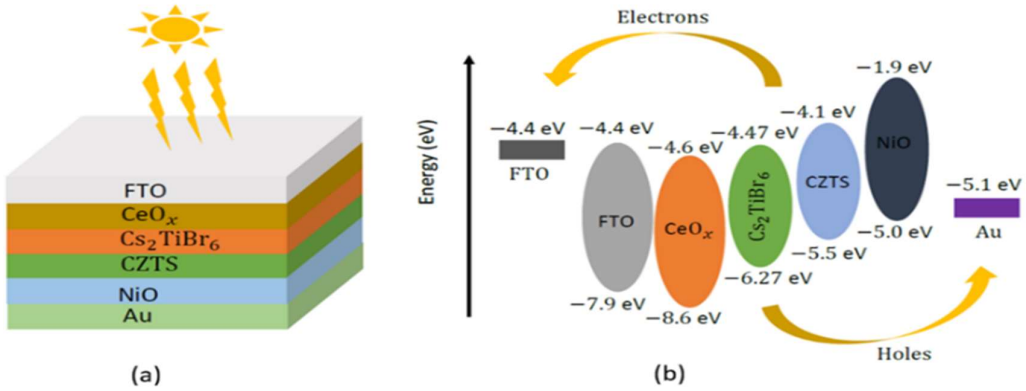

Fig. 1. Schematic diagram of the solar cell structure, (b) Energy level diagram of the PSC.

B. Device Input Parameter

Table I presents the basic physical parameters of the materials as sourced from relevant published works [8, 22, 23].

This study is aimed at investigating the double-HTL PSC with FTO/CeOx/Cs_2TiBr_6/CZTS/NiO/Au configuration. However, the single-HTL counterpart devices (FTO/CeOx/Cs_2TiBr_6/CZTS/Au and FTO/CeOx/Cs_2TiBr_6/NiO/Au), were simulated to support the choice for the double-HTL device. The CZTS-based single-HTL device has the potential to suffer from relatively high defect density at interfaces, leading to charge recombination. Similarly, the NiO-based single-HTL device is prone to interface mismatch with some perovskite absorbers, which can cause recombination to limit open circuit voltage (V_{OC}). Conversely, using the double HTL (CZTS/NiO) creates a graded, stepwise energy-level alignment, which enhances hole extraction, minimizes recombination losses, and promotes stability relative to the utilization of either CZTS or NiO alone. This potentially leads to higher PCE and longer device lifetime.

The interface layer parameters are presented in Table II. The work functions of FTO and Au are 4.4 and 5.1 eV, respectively [4, 24]. The simulations were performed under an AM 1.5G illumination with an incident light power density of 1000 W/m^2 at 1×10^6 Hz, a scan voltage range of 0-1.5 V, and an operating temperature of 300 K. In order to determine the optimal parameters for the enhanced device performance, the thickness of all layers, the defect of the absorber, all interface-defects, and cross section of electrons, and the series resistance of the prototype device were varied.

Table I. Parameters used in PSC solar cell simulation

Parameter	Layer				
	CZTS [8]	NiO [16, 17]	Cs_2TiBr_6 [8]	CeO_x [8]	FTO [8]
Thickness (μm)	0.1	0.2	0.5	0.1	0.5
E_g (eV)	1.4	3.8	1.8	3.5	3.5
χ (eV)	4.1	1.46	4.47	4.4	4.3
ε_r	9	10	10	9.0	9.0
N_C (cm^{-3})	2.2×10^{18}	2.8×10^{19}	6.0×10^{19}	1.0×10^{20}	2.2×10^{18}
N_V (cm^{-3})	1.8×10^{18}	1×10^{19}	2.0×10^{19}	2.0×10^{21}	1.8×10^{19}
μ_n (cm^2V^{-1} s^{-1})	100	200	4.4	100	200
μ_p (cm^2V^{-1} s^{-1})	12.5	20	2.5	25	10
e V_{th} (cm/s)	1×10^7	1×10^7	1×10^7	1×10^7	1×10^7
h V_{th} (cm/s)	1×10^7	1×10^7	1×10^7	1×10^7	1×10^7
N_D (cm^{-3})	0	0	1×10^{19}	1×10^{16}	2×10^{19}
N_A (cm^{-3})	1×10^{16}	1×10^{16}	1×10^{19}	0	0
N_t (cm^{-3})	1×10^{15}	1×10^{14}	1×10^{14}	1×10^{15}	1×10^{15}
σ (e) (cm^2)	1×10^{-15}	1×10^{-15}	1×10^{-15}	1×10^{-15}	1×10^{-15}
σ (h) (cm^2)	1×10^{-15}	1×10^{-15}	1×10^{-15}	1×10^{-15}	1×10^{-15}

Table II. Interface defect parameters for the various device simulations

Parameters	CeO_x/Cs_2TiBr_6	Cs_2TiBr_6/CZTS	CZTS/NiO
Defect type	Neutral	Neutral	Neutral
σ (e) (cm^2)	1×10^{-19}	1×10^{-19}	1×10^{-19}
σ (h) (cm^2)	1×10^{-19}	1×10^{-19}	1×10^{-19}
Energetic distribution	Single	Single	Single
Energy level with respect to E_v (eV)	0.60	0.60	0.60
Characteristic energy (eV)	0.10	0.10	0.10
Interface defect density (cm^{-2})	1×10^{13}	1×10^{13}	1×10^{10}

III. Results And Discussion

A. PV performance of the prototype PSCs

Fig. 2 illustrate the energy band plots of the various PSCs. In the CZTS HTL-based PSC (see Fig. 2a), the valence band maximum (VBM) of Cs_2TiBr_6 lies significantly below that of CZTS, creating a valence band offset of about 0.77 eV. This introduced a moderate barrier to hole extraction, which restricted hole transport from the Cs_2TiBr_6 absorber into the CZTS layer.

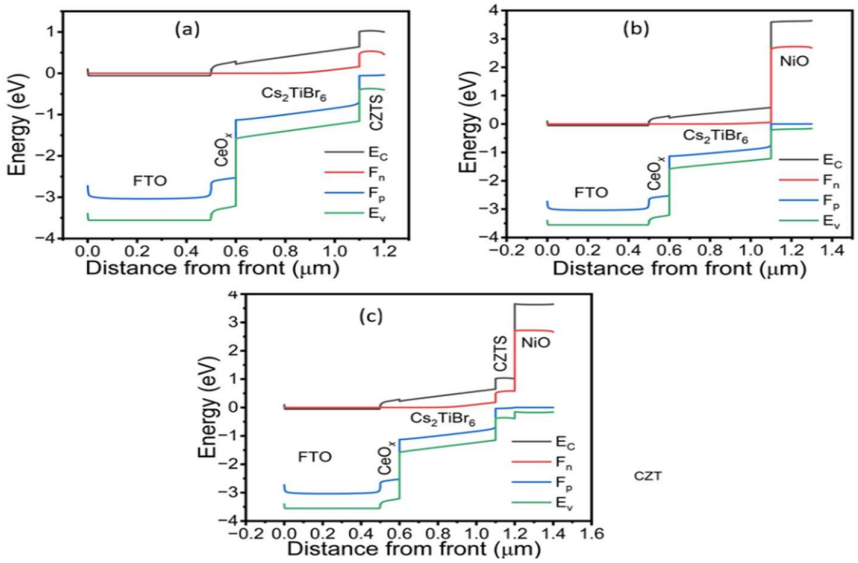

Fig. 2. Energy band plots of the (a) CZTS-based PSC, (b) NiO-based PSC, (c) CZTS/NiO-based PSC.

Although holes could still overcome this barrier under forward bias, the band discontinuity promoted interface recombination, reducing both the V_{OC} and the FF. Moreover, CZTS has a relatively narrow bandgap (1.4 eV) and a shallower conduction band (EC) that is not much higher than that of Cs_2TiBr_6. This weakened its electron-blocking ability, allowing electrons to leak into the HTL. This combination of hole extraction barrier and weaker electron blocking has the potential to produce a modest PV performance in the CZTS HTL-only device.

Fig. 3b depicts the energy band alignment of the no-HTL-based PSC. The valence band offset at the Cs_2TiBr_6/NiO interface is ~1.0 eV compared to the CZTS-based PSC. This severe misalignment created a strong barrier to hole extraction, causing the hole to accumulate at the interface. A clear step between the Cs_2TiBr_6 perovskite VBM and NiO VBM could be seen, signifying the high barrier that directly limited current transport. As a result, both the V_{OC} and J_{SC} are expected to be strongly reduced because recombination dominates at this constraint. On the advantage side, NiO has a wide bandgap (3.8 eV) and a very high conduction band edge, which provides excellent electron blocking. This explains why the FF is expected to be relatively high despite the low J_{SC} and V_{OC}, since the diode characteristics remained intact and leakage current was minimized.

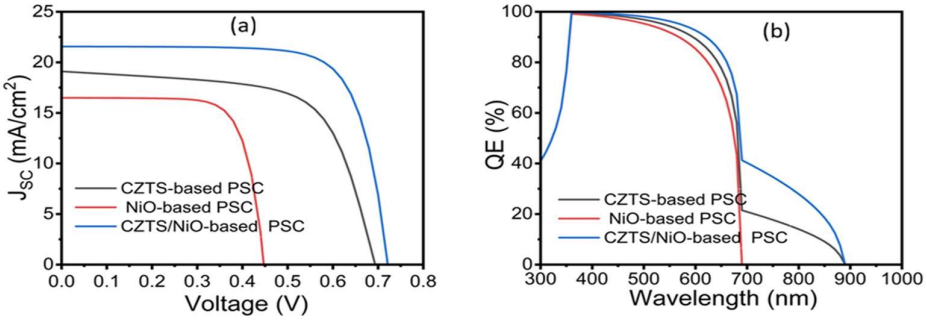

Fig. 3. J-V curves for the prototype PSCs based on Cs_2TiBr_6 perovskite absorber, (b) QE plots.

Table III. PV performance metrics of the prototype PSCs.

Solar cell	V_{OC} (V)	J_{SC} (mA/cm^2)	FF (%)	PCE (%)	Reference
FTO/CeO_x/Cs_2TiBr_6/CZTS/NiO/Au	0.72	21.56	74.69	11.62	This work
FTO/CeO_x/Cs_2TiBr_6/CZTS/Au	0.69	19.10	65.47	8.67	This work
FTO/CeO_x/Cs_2TiBr_6/NiO/Au	0.45	16.49	74.26	5.49	This work

The CZTS/NiO double HTL-based PSC (see Fig. 2c) illustrated how the stack arrangement of the two HTLs mitigated the limitations of the individual layers. In this configuration, the large 1.0 eV barrier is split into two smaller steps: 0.77 eV between Cs_2TiBr_6 and CZTS, and 0.23 eV between CZTS and NiO. This band alignment allowed holes to flow more smoothly across successive interfaces rather than facing a single, abrupt barrier. The band diagram clearly illustrated a stepwise transition that reduced energetic losses during transport. This smooth band alignment has the potential for a better balance of charge extraction and suppression of carrier losses to produce superior device performance.

The FTO/CeO_x/Cs_2TiBr_6/NiO/Au (or NiO HTL-based) PSC showed the weakest PV performance with a V_{OC} of 0.45 V, J_{SC} of 16.49 mA/cm^2, and lower PCE of 5.49% (see Table III, and Fig. 3a). This poor performance could be attributed to the large valence-band offset of about 1.0 eV between Cs_2TiBr_6 and NiO, which created a strong barrier to hole extraction. The holes accumulated at this interface lead to enhanced recombination, causing a drastic reduction in V_{OC}. This barrier also limited current collection, explaining the relatively low J_{SC}. Interestingly, the FF remained high (74.26%) due to the wide bandgap of NiO and the deep conduction band that provided strong electron blocking to suppress leakage current. Thus, NiO alone acted as an effective electron-blocking layer but was highly unsuitable as a direct hole-transport layer for Cs_2TiBr_6 because of the severe band misalignment (see Fig. 3b).

The FTO/CeO_x/Cs_2TiBr_6/CZTS/Au (or CZTS HTL-based) device performed better, yielding a higher V_{OC} of 0.69 V, J_{SC} of 19.10 mA/cm^2, and a PCE of 8.67%, though the FF dropped significantly to 65.47%. Compared with the NiO-based device, the barrier for hole extraction is smaller at the Cs_2TiBr_6/CZTS interface (≈0.77 eV), which improved both V_{OC} and J_{SC}. The decrease in FF could be a result of the narrower bandgap (1.4 eV) of CZTS and relatively shallow conduction band, which weakened its electron-blocking ability. This allowed electron leakage into the HTL, thereby increasing recombination that raises the saturation current density and lowers the diode quality.

The FTO/CeO_x/Cs_2TiBr_6/CZTS/NiO/Au (or CZTS/NiO double HTL-based) device offered the best PV performance, achieving a superior V_{OC} of 0.72 V, J_{SC} of 21.56 mA/cm^2, FF of 74.69%, and PCE of 11.62%. This configuration benefits from splitting the large Cs_2TiBr_6-NiO valence-band offset into two smaller steps, viz, 0.77 eV at the Cs_2TiBr_6/CZTS interface

and 0.23 eV at the CZTS/NiO interface. This produced a more favourable energetic hole extraction, while NiO still provided strong electron blocking behind CZTS. The placement of CZTS next to Cs_2TiBr_6 absorber also improves chemical compatibility and reduces interfacial recombination compared with the direct NiO contact.

Fig. 4b demonstrates the QE of the various prototype PSCs. The CZTS/No double HTL-based PSC showed the highest QE (above 90%) across the entire visible spectrum (350–650 nm) and maintained a strong response up to 750 nm. This broad and high spectral response indicated excellent light harvesting and efficient carrier extraction, consistent with its highest measured J_{SC} (21.6 mA/cm^2). The smooth alignment of HTL reduced recombination losses and ensured efficient hole transport, which is reflected in the superior QE.

1) Carrier Generation and Recombination

Fig. 4a-b depict the carrier generation rate for the various cells. The generation rate was dominated at the front (0.6 µm) of the Cs_2TiBr_6 absorber (i.e., at the CeO_x/Cs_2TiBr_6 interface), followed by an exponential drop with depth to the back (1.1 μm) of the absorber layer. This behavior applied to all three devices. However, there is a clear distinction in the region 1.1–1.4 µm. The best two performing devices (CZTS- and CZTS/NiO-based cells) exhibited another generation around 1.1 μm in front of the CZTS layer (i.e., at the Cs_2TiBr_6/CZTS interface) (see Fig. 4a), followed by a gradual decline in the CZTS layer (applicable to the CZTS- and CZTS/NiO-based cells) and an abrupt drop in the NiO layer (applicable only to the CZTS/NiO-based cell). This behavior supports the better PV performance of the CZTS-based cell and the superior outcome of the CZTS/NiO double HTL-based cell. The CZTS HTL acts as the supporting/second absorber and carrier generation layer, which enhances the population of carriers. Meanwhile, the NiO-based cell did not demonstrate another generation at the Cs_2TiBr_6/NiO front, thus supporting its least PV performance. The NiO HTL did not absorb light, so a strong hole-extraction barrier at Cs_2TiBr_6/NiO reduced the internal field near the back to prevent the long-wavelength carriers generated deeper in the Cs_2TiBr_6 absorber from being separated and collected.

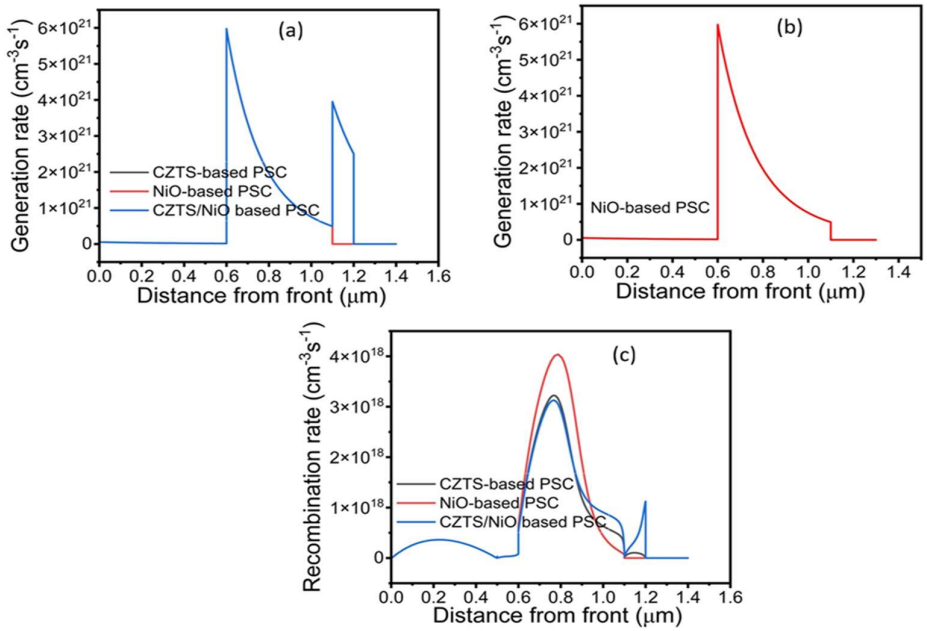

Fig. 4. (a) Carrier generation rate for the various PSCs, (b) Carrier generation rate for the NiO-based PSC, (c) Carrier recombination rate for the various PSCs.

Fig. 4c depicts the carrier recombination profiles. All devices showed peak recombination in the Cs_2TiBr_6 absorber (Cs_2TiBr_6/CZTS region), where both carrier densities are high. The NiO-based cell exhibited the highest peak, reflecting hole accumulation against the barrier and enhanced SRH recombination at (or near) the Cs_2TiBr_6/NiO interface. This effect directly explained its lower V_{OC} and J_{SC}. The CZTS-based device demonstrates a slightly lower but still pronounced recombination peak. Here, the higher interface-trap density at Cs_2TiBr_6/CZTS and weaker electron blocking in CZTS elevated leakage and interfacial SRH, which affected the FF (S-curve tendency) and lowered V_{OC}. The CZTS/NiO bilayer exhibited the lowest recombination peak and a higher stepwise/ gradual decay (around 0.9 µm), supporting its superior PV output.

B. Effect of layer thickness

1) Influence of thickness of the CeOx ETL layer

The negligible impact of increasing the CeO_x layer thickness in the FTO/CeO_x/Cs_2TiBr_6/CZTS/NiO/Au PSC is displayed in Fig. 5. The V_{OC} and J_{SC} remain consistent at 0.72 V and 21.56 mA/cm^2, respectively (see Fig. 6a), across the

thickness range of 0.1–0.2 m. Fig. 5 shows a negligible impact of increasing the CeO_x layer thickness in the FTO/CeO_x/Cs_2TiBr_6/CZTS/NiO/Au PSC. The V_{OC} and J_{SC} remain consistent at 0.72 V and 21.56 mA/cm^2, respectively across the thickness range of 0.1 to 0.2 m (see Fig. 6a). However, the FF decreased negligibly, ranging from 74.67 to 74.64%, while the PCE varied marginally, ranging from 11.62 to 11.61%. This negligible difference in device performance metrics can be ascribed to the wide bandgap of CeO_x, which rarely absorbs incident light. Moreover, the conduction band offset with Cs_2TiBr_6 was already close to the ideal level for efficiently extracting electrons. Additionally, there was no significant increase in series resistance within this thickness range, nor were there changes in the interfacial recombination dynamics that primarily influence performance at the back contact. These findings suggest a good tolerance for the ETL design to variations in thickness.

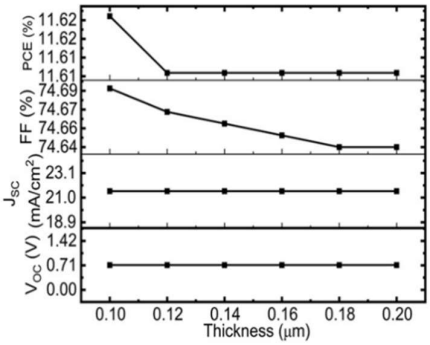

Fig. 5. (a) Variation of V_{OC}, J_{SC}, FF, and PCE with CeO_x layer thickness.

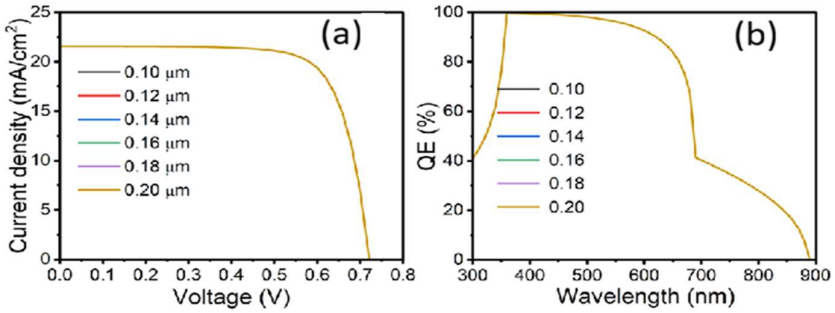

Fig. 6. (a) J-V curves with varying thickness of the CeOx layer, (b) QE plots.

Fig. 6b depicts the QE spectra for various CeO_x thicknesses in the range $0.1 - 0.20\ \mu m$. The QE reached 100% within a $350 - 400\ nm$ range and then gradually decreased to 0% at $450\ nm$, which is $900\ nm$ from QE. This suggests that changing the thickness of CeO_x did not affect the absorption of light or the effectiveness of the carriers collected. Since QE represents the percentage of incoming photons that is converted into charge carriers, the identical QE curves indicate that photon absorption, carrier generation, and collection did not change. This effect produced a steady value of J_{SC} (see Fig. 6a) within the range of thickness tested.

2) Effect of thickness of the absorber layer

The effects of the absorber layer thickness on the PV parameters are depicted in Figs. 6 and 8. An increase in the thickness of the Cs_2TiBr_6 absorber (0.1–0.5 μm) enhanced the J_{SC}, while the V_{OC} remained stable and the FF experienced a slight decline. This led to an increase in PCE. A very thin absorber (0.1–0.2 μm) does not have sufficient optical path to effectively capture long-wavelength photons, which limits J_{SC} to a range of 17.41 to 19.25 mA/cm^2 (see Figs. 7, 8a) despite having good electrostatic properties. This resulted in a modest PCE of 9.71 to 10.57%. The device starts to absorb more of the red and near-infrared light, and the collection region expands as the thickness increases (0.30–0.50 μm), causing J_{SC} to rise steadily from 20.38 to 21.56 mA/cm^2. The V_{OC} remains consistently at 0.72 V throughout the thickness range because the built-in potential, interfacial energetics (such as CeO_x/Cs_2TiBr_6 and CZTS/NiO), and the recombination current influenced by interface traps did not change significantly with moderate thickness adjustments. The slight drop in FF (78.08–74.69%) with an increase in thickness indicates a rise in bulk transport losses – longer distances for carriers to travel, a bit more series resistance, and increased chances for SRH recombination within the absorber bulk. The PCE improved from 9.71 to 11.62%, with the optimal thickness hinting at 0.5 μm.

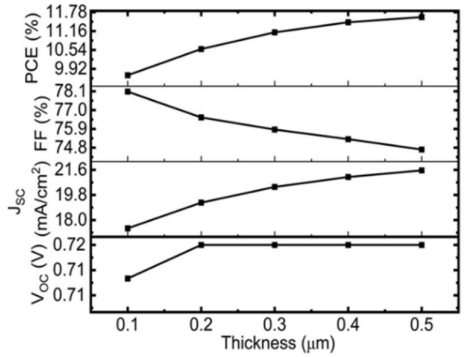

Fig. 7. (a) Variation of V_{OC}, J_{SC}, FF, and PCE with the thickness of the absorber-layer.

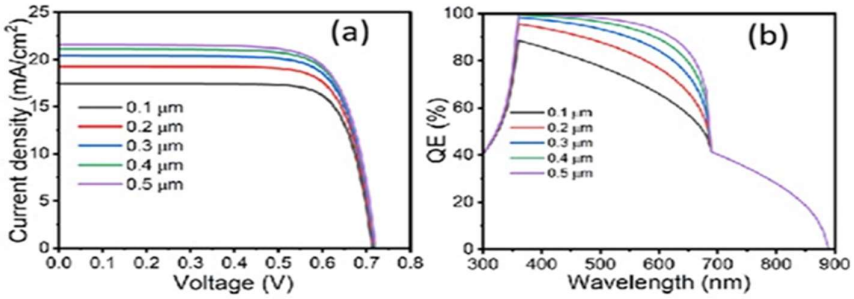

Fig. 8. (a) J-V curves with varying thickness of the absorber layer, (b) QE plots.

Fig. 8b illustrates QE curves under varying absorber layer thickness. The QE across the visible spectrum is boosted by an increase in thickness (0.1–0.5 μm). This is particularly noticeable in the 400-700 nm range, where the thinner absorbers (0.1–0.2 μm) tend to underperform, losing carriers due to back reflection and recombination. The long-wavelength cutoff is close to the band-edge (E_g = 1.8 eV, λ = 690 nm), suggesting that while the thicker films improved the QE to 100% around 400 nm, they did not extend the response beyond 750 nm. Since J_{SC} is proportional to the integral of QE(λ) multiplied by the photon flux Φ(λ), the increased area under the QE curve directly led to the observed increase in J_{SC} (see Fig. 8a).

3) Influence of thickness of the CZTS layer

Figs. 9a and 10 demonstrate the impact of CZTS thickness on the performance of the FTO/CeO_x/Cs_2TiBr_6/CZTS/NiO/Au PSC. An increase in thickness (0.4–1μm) showed a constant V_{OC} (0.74 V), a monotonic rise in J_{SC} (28.27–31.26 mA/cm^2), a slightly varied FF (77.43–77.31%), and an appreciable PCE increase (16.16–17.96%). The constant value of V_{OC} indicated a steady electric field across the Cs_2TiBr_6/CZTS junction. The steady gains in J_{SC} (see Fig. 10b) suggested improved light absorption and carrier generation, hole extraction, and reduced back-side recombination with increasing CZTS thickness. A thicker CZTS layer enhanced band bending at the Cs_2TiBr_6/CZTS interface, screened the downstream NiO step, and lowered the probability that the holes generated deeper in Cs_2TiBr_6 were lost at the back contact. The nearly unchanged FF could be attributed to a slight increase in bulk recombination and a negligible increase in carrier transport distance. The significant increase in PCE was driven mainly by an increase in J_{SC}. Practically, this finding revealed a beneficial electrical effect of thicker CZTS because of better selectivity and weaker interfacial SRH at the Cs_2TiBr_6/CZTS interface.

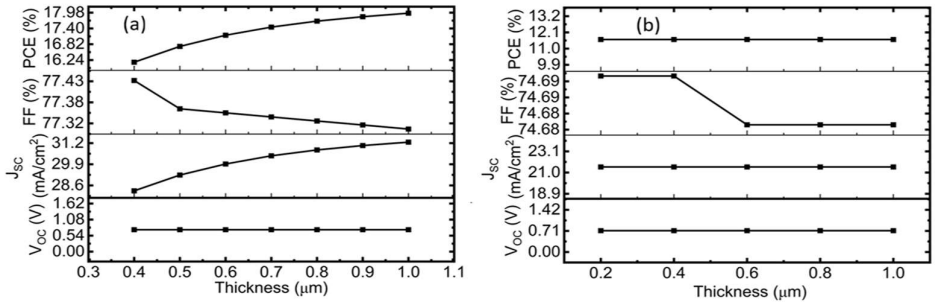

Fig. 9. Variation of V_{OC}, J_{SC}, FF, and PCE with the thickness of the (a) CZTS, (b) NiO HTLs.

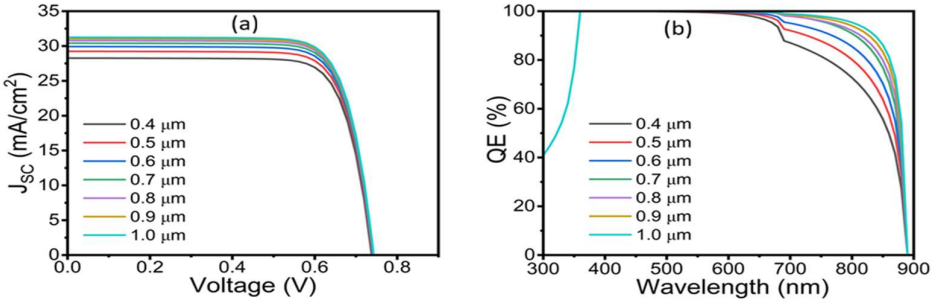

Fig. 10. (a) J-V curves for varying thickness of the CZTS HTL, (b) QE plots.

Fig. 10b illustrated a consistent boost in QE in the $700-880\,nm$ spectrum range with increased thickness of CZTS ($0.4-1\,\mu m$). The significant improvement occurred in the longer wavelength, where photons could penetrate deeper into the CZTS which played the dual role of carrier generation and hole transport. The increase in QE with thickness support the increasing J_{SC} (see Figs. 9a, and 10a) due to the increased absorption of photons and carrier generation.

4) Impact of the thickness of the NiO layer

Adjusting the thickness of NiO ($0.20-1.0\,\mu m$) did not change the performance (see Figs. 9b, and 11). The V_{OC} stayed at 0.72 V, J_{SC} at 21.56 mA/cm^2, FF at 74.70% (although with a negligible change from 74.69–74.68%), and the PCE remained unchanged at 11.62%. This is because the NiO primarily served as an electron-blocking layer behind CZTS. It is optically transparent due to its large bandgap of 3.8 eV, meaning it does not absorb photons or facilitates improving J_{SC}. This layer does not make direct junction with the Cs_2TiBr_6 absorber, suggesting that it did not directly participate in the built-in field to influence the V_{OC}. The steady value of FF could be attributed to the absence of the recombination effect.

Fig. 11b showed the QE results. It could be seen that QE curves overlapped with varying NiO thickness. This supports the constant value of the J_{SC} because photon absorption, carrier generation, and separation did not change with varying thickness.

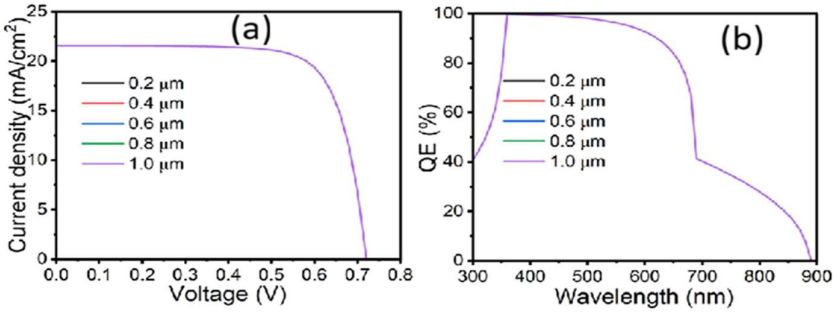

Fig. 11. (a) J-V curves with varying thickness of the No layer, (b) QE plots.

C. Influence of defect density on the PSC

1) Defect density of the CeO_x layer

Figs. 12 and 13 demonstrate that variation in defect density of CeO_x ETL (10^{14}–10^{18} cm^{-3}) had a negligible effect on the performance metrics. The V_{OC} remained constant at 0.72 V, while J_{SC} remained the same at 21.56 mA/cm^2 up to 10^{17} cm^{-3}, but dropped slightly to 21.52 mA/cm^2 at 10^{18} cm^{-3}. Similarly, the FF remained the same at 74.69% up to 10^{17} cm^{-3}, but dropped negligibly to 74.68% at 10^{18} cm^{-3}. In the same vein, PCE stayed unchanged at 11.62% up to 10^{16} cm^{-3}, then declined slightly from 11.61–11.59% between 10^{17} and 10^{18} cm^{-3}. The negligible change in performance could be ascribed to the moderate increase in SRH recombination. There was no significant impact on optical absorption that would affect the J_{SC} or the built-in potential that would impact the V_{OC}. Only a high defect density of 10^{18} cm^{-3} would slightly increase recombination and series/transport losses, thereby reducing J_{SC} and PCE by roughly 0.1 to 0.3%. This means that CeO_x can tolerate a wide range of bulk defects (10^{14}–10^{17} cm^{-3}).

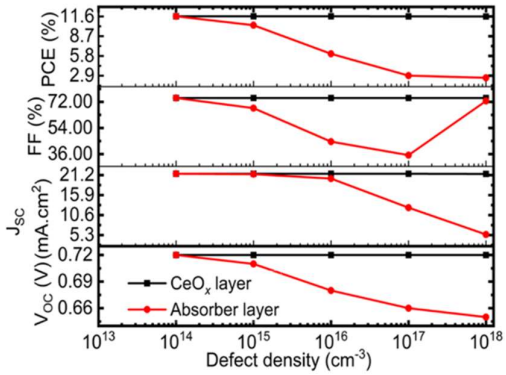

Fig. 12. (a) Variation of V_{OC}, J_{SC}, FF and PCE with defect density of the CeO_x- and absorber-layer.

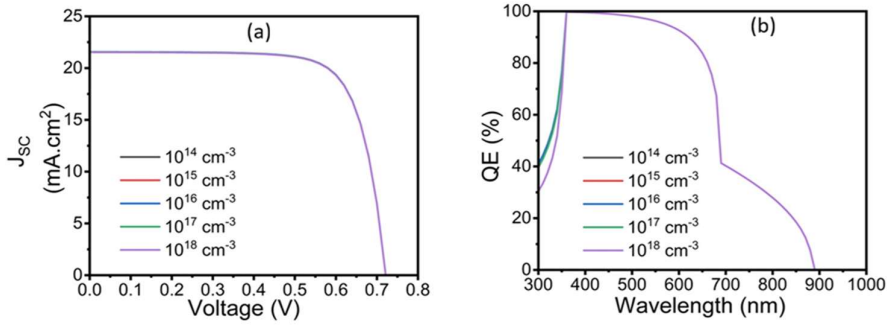

Fig. 13. (a) J-V curves with varying defect density of the CeO_x-layer, (b) QE plots.

The QE results (see Fig. 13b) showed overlapping curves supporting a constant value of J_{SC} for the range of defect density (see Figs. 12 and 13a). The slight drop in J_{SC}, and hence PCE at 10^{18} cm^{-3}, could be attributed to the slight drop in QE in the UV region (300–350 nm). A few carriers excited in this region could not be collected.

2) Defect density of the absorber layer

Fig. 12 reveals that increasing the bulk defect density (10^{14}–10^{18} cm^{-3}) of the Cs_2TiBr_6 absorber significantly degrades the PV performance. The PCE dropped drastically (11.62–2.59%) due to the severe degradation of the three diode parameters. The V_{OC} reduced (0.72–0.65 V) as the minority-carrier lifetime was shortened, enhancing the recombination current J_0. The J_{SC} dropped (21.56–5.44 mA/cm^2, Figs. 12, and 14a) because the carrier diffusion length declined, so that a large fraction of photocarriers recombined before reaching the selective contacts. The FF deteriorated sharply (74.69–35.26%) up to 10^{17} cm^{-3} due to enhanced SRH recombination, larger ideality factor, and field screening. The sharp increase in FF to 72.64% at 10^{18} cm^{-3} could be attributed to a mathematical artifact of a severely current-limited diode, despite the low power output and reduced PCE (2.59%). These results indicate that the absorber bulk defect density is the dominant factor. Therefore, retaining a defect density $\lesssim 10^{14-15}$ cm^{-3} is essential for optimal optical performance. In practice, this means that higher stoichiometry, grain-boundary passivation, mild post-annealing, and controlled oxygen atmosphere are vital to prolong carrier lifetime, ensuring higher V_{OC}, J_{SC}, and FF.

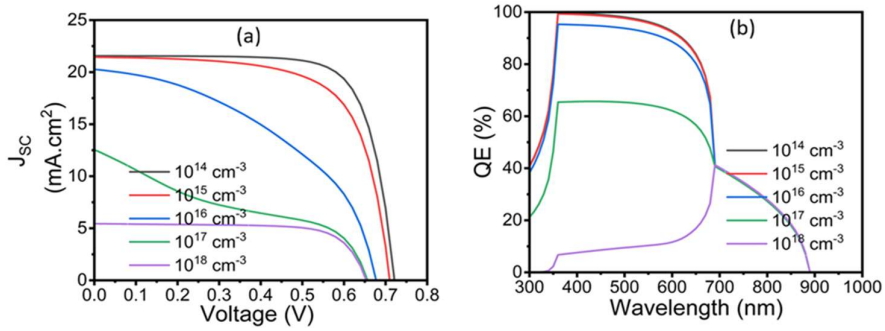

Fig. 14. (a) J-V curves with varying defect density of the absorber layer, (b) QE plots.

The QE results showed a decrease in the visible range (350–680 nm) as the Cs_2TiBr_6 absorber bulk defect density increased, supporting the decreased J_{SC} (see Fig. 14b). Higher defect density increases SRH recombination, shortens carrier lifetime, and reduces the diffusion length. This caused carriers generated by long-wavelength photons to recombine before reaching the contacts.

3) Defect density of the CZTS layer

Figs. 15 and 16a reveal that raising the bulk defect density of the CZTS layer exhibited a considerable effect on the performance, especially at higher defect densities 10^{16} and 10^{17} cm^{-3}. The significant decline in PCE at the higher defects is due to a collapse in the FF. The V_{OC} remained the same (0.72 V) between 10^{14}–10^{16} cm^{-3}, and the J_{SC} stayed at 21.56 mA/cm^2, with just a slight drop in FF (74.72–74.44%). This suggested that moderate CZTS traps did not affect light absorption or carrier extraction. However, higher defects (10^{17}–10^{18} cm^{-3}) led to a significant drop in FF (72.20–65.52%), along with a small decrease in J_{SC} ($21.50 - 20.99\ mAcm^2$), which degraded the PCE down to 9.76%. This could be ascribed to deep traps in the CZTS layer that promoted SRH recombination of minority electrons that reached the CZTS. This raised the ideality factor and J_0 (leading to a drop in V_{OC}) and caused trap-limited hole transport (increasing series/transport resistance). All of these combined to lower FF and slightly reduce J_{SC}. Therefore, a defect density of $< 10^{16}$ cm^{-3} is required to maintain PV performance.

The QE results demonstrated overlapping curves, which is consistent with the steady value of J_{SC} (21.56 mA/cm^2) at a defect of $< 10^{17}$ cm^{-3} (see Fig. 16b). The slight drop in J_{SC}, and hence PCE at 10^{18} cm^{-3}, could be attributed to the slight drop in QE in the UV region (300–350 nm). This is because the carriers generated in this region could not be collected.

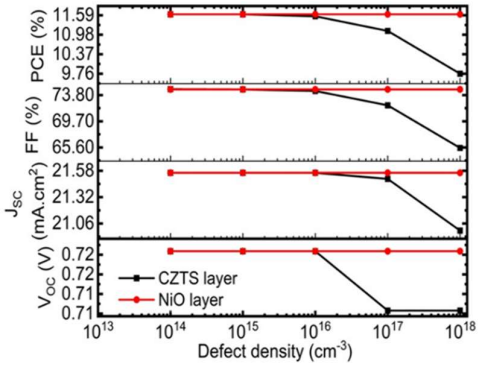

Fig. 15. Variation of V_{OC}, J_{SC}, FF, and PCE with defect density of the CZTS- and NiO-layer.

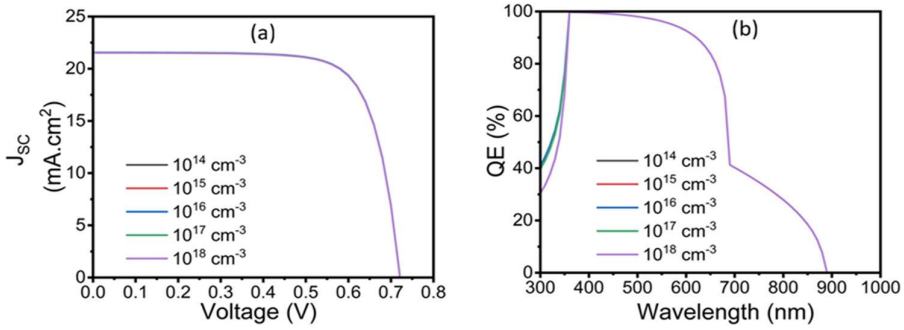

Fig. 16. (a) J-V curves with varying defect density of the CZTS-layer, (b) QE plots.

4) Defect density of the NiO layer

Over the past decades, the defect density of NiO in the range (10^{14}–10^{18} cm^{-3}) has been reported to have a negligible impact on PV performance [25, 26]. In the same vein, Figs. 15 and 17a displays steady metrics (V_{OC} = 0.72 V, J_{SC} = 21.56 mA/cm^2, FF = 74.69%, and PCE = 11.62%) over the tested range of defects. This suggested that NiO acted primarily as a wide-bandgap electron blocker at the back contact. The built-in field established at the Cs_2TiBr_6/CZTS junction made the NiO layer quasi-neutral, so that increasing its trap density did not affect the band offsets or the front-side recombination that could influence V_{OC} and J_{SC}. Optically, the NiO layer was transparent, meaning that the QE and, consequently, J_{SC}, remained unaffected. The QE results (see Fig. 17b) illustrated overlapping curves, which translated the steady J_{SC} observed in the simulations. The slight difference in QE in the long wavelength (700–890 nm) was too small to cause a noticeable impact on carrier generation and extraction, which could affect the J_{SC} (see Fig. 17a).

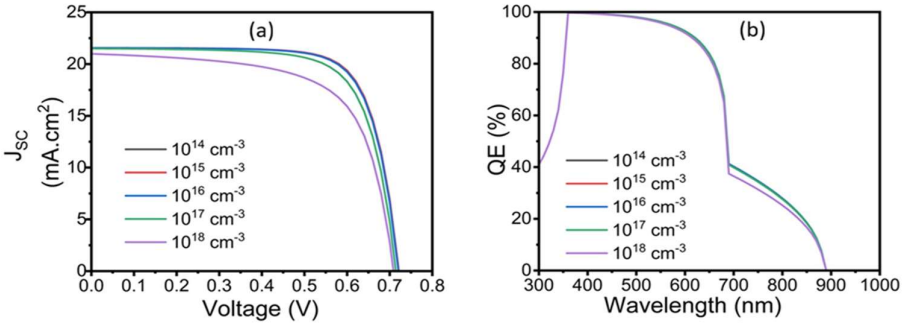

Fig. 17. (a) J-V curves with varying defect density of the NiO-layer, (b) QE plots.

D. Impact of interface defect density on PV performance

1) Defect density of the CeOx/absorber interface

Figs. 18 and 19a reveal that an increase in defect density at the CeO_x/Cs_2TiBr_6 interface (10^{10}–10^{15} cm^{-2}) produced stable PV performance (V_{OC} = 0.72 V, J_{SC} = 21.56, FF = 74.71%, PCE = 11.62%) up to an interface defect of 10^{15} cm^{-2}. The performance began to drop, specifically for the FF (74.50–72.82%) at 10^{14} and 10^{15} cm^{-3}. Also, the J_{SC} slightly decreased to 21.48 mA/cm^2, while the V_{OC} remained the same (0.72 V). This suggested that the front-interface possesses some SRH traps that: (i) slightly increased interfacial recombination under forward bias, which raises the diode ideality and leakage, leading to decreased FF, and (ii) hindered the collection of short-wavelength carriers generated near the CeO_x layer, causing a minor drop in J_{SC}.

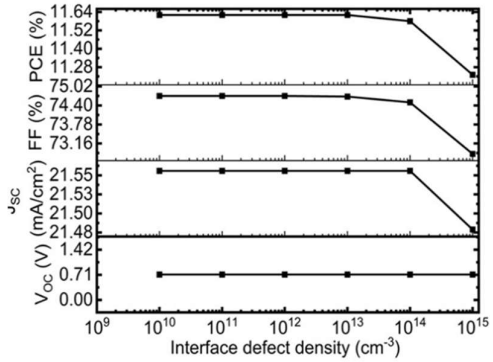

Fig. 18. (a) Variation of V_{OC}, J_{SC}, FF, and PCE with defect density of the CeO_x/Cs_2TiBr_6 interface.

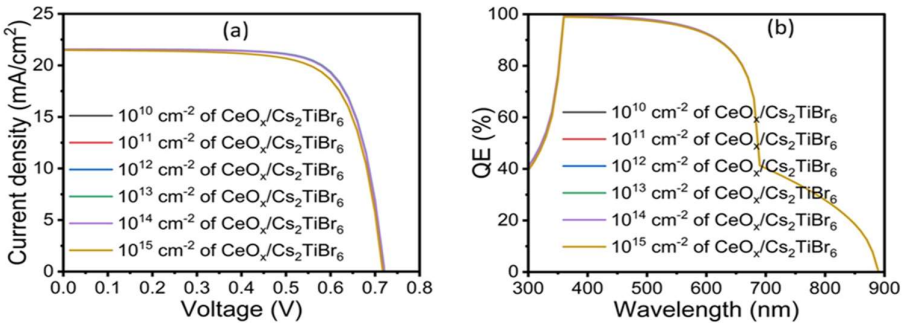

Fig. 19. (a) J-V curves with varying defect density of the CeO_x/Cs_2TiBr_6 interface, (b) QE plots.

The constant value of V_{OC} indicated that the recombination current J_0 was mainly influenced by the other interfaces (Cs_2TiBr_6/CZTS and CZTS/NiO). These results suggest that maintaining the interface-face defect below 10^{13} cm^{-2} preserves the neutrality of the CeO_x/perovskite interface, resulting in enhanced performance. Some effective practical strategies to mitigate this include using small oxygen plasma or UV-ozone treatments to reduce CeO_x oxygen-vacancy states, applying ultrathin passivation layers (PEIE and LiF), growing smooth-surface CeO_x with the ALD synthesis method, and performing mild surface treatments on the perovskite before depositing the NiO ETL.

The QE spectra displayed overlapping curves consistent with the equivalent J_{SC} output (21.56 mA/cm^2) for varying interface defect densities (see Fig. 19b). This indicates that light absorption, carrier generation, and extraction remain unchanged. The slight QE depression observed in the short-wavelength (300–370 nm) region at 10^{15} cm^{-2} supported the minor change in J_{SC} (21.48 mA/cm^2), suggesting that a few carriers generated in this region recombined at the additional trap sites and could not be extracted.

2) Defect density of the absorber/CZTS interface

Table IV and Fig. 20 show the influence of increasing defect density of the Cs_2TiBr_6/CZTS interface on PV performance. An increase in interface-defects (10^{10}-10^{15} cm^{-2}) changed the dynamic of the device from a high-voltage, low-loss junction into a recombination-limited one, with V_{OC} and FF severely affected while J_{SC} remained unchanged (see Table IV and Fig. 20). Interface-defects $\leq 10^{12}$ cm^{-2} provided a steady value of J_{SC} (21.56 mA/cm^2) and decreasing PCE (15.66–13.62%). This implies a very high V_{OC} and FF, consistent with a trap-free, selective interface where interfacial SRH recombination is negligible and the quasi-Fermi-level splitting is large. Furthermore, an increase in the interface defect density (10^{13}–10^{15} cm^{-2}) increases the SRH recombination, J_0, and the diode ideality factor, resulting in a decrease in the V_{OC} (0.72–0.51 V) and FF (74.69–62.58%). The J_{SC} remained nearly the same (21.56–21.50 mA/cm^2) because light absorption and carrier extraction were unchanged, but the PCE declined significantly (11.62 - 6.81%). This implied that the absorber/CZTS interface is the major recombination channel at higher interface defects. The findings revealed that keeping the interface-defect density 10^{13} cm^{-2} is critical for boosting device performance. In practice, the defect can be reduced by: (i) chemical passivation of the Cs_2TiBr_6 perovskite surface before deposition of CZTS, (ii) inserting ultrathin interlayers to decouple traps and tune the valence-band offset, (iii) improving CZTS film quality/stoichiometry and modest HTL doping to strengthen band bending and reduce carrier pile-up. These approaches will suppress interfacial SRH and lower the J_0 to ensure high V_{OC} and FF similar to the values obtained from this simulation.

The QE results depict overlapping curves, which support the steady value of J_{SC} over the tested range of the interface defect because light absorption, carrier generation, and extraction did not change (see Fig. 20).

Table. IV. Variation of PV parameters with defect density of the absorber/CZTS interface.

Interface defect density (cm^{-2})	V_{OC} (V)	J_{SC} (mA/cm²)	FF (%)	PCE (%)
10^{10}	-	21.56	-	15.66
10^{11}	-	21.56	-	15.33
10^{12}	-	21.56	-	13.62
10^{13}	0.72	21.56	74.69	11.62
10^{14}	0.61	21.56	70.86	9.39
10^{15}	0.51	21.50	62.58	6.81

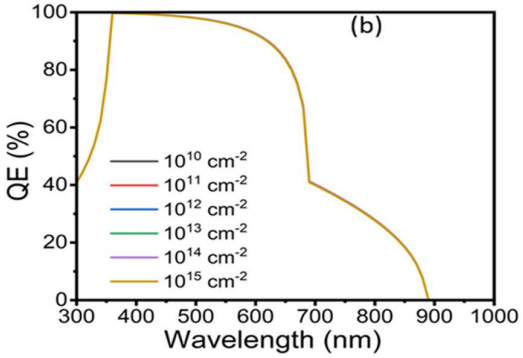

Fig. 20. QE of the with varying defect density of the absorber/CZTS interface.

3) Defect density of the CZTS/NiO interface

Figs. 21 and 22 reveal a noticeable degradation in PV performance at higher interface defect densities ($\leq 10^{13}$ cm^{-2}), where the PCE begins to drop from its steady value of 11.62%. The progressive degradation in performance began primarily with a slight decline in FF (74.69–74.68%) between defects of 10^{12} and 10^{13} cm^{-2}, while the values of V_{OC} (0.72 V) and J_{SC} (21.56 mA/cm^2) remain the same up to defects of $\leq 10^{14}$ cm^{-2}. The slight decrease in PCE (11.61–11.50%) between 10^{13} and 10^{14} cm^{-2} could be ascribed to the small decrease in FF (74.68–74.41%). Meanwhile, the higher PCE degradation (11.50–10.86%) recorded at the larger interface-defect level (10^{15} cm^{-2}) results from the combined decreases in V_{OC} (0.72–0.71 V), J_{SC} (21.56–21.54 mA/cm^2), and FF (74.41–70.93%). The additional back-interface traps increased the SRH recombination and raised the ideality factor/leakage (higher J_0), which initially lowered FF. The V_{OC} dropped slightly because the dominant recombination path was still found in the absorber/CZTS interface, and the built-in field was largest at this junction. The nearly steady value of J_{SC} could be traced to the steady photon absorption and carrier generation, as supported by the overlapping curves of the QE (see Fig. 22b). These findings revealed that keeping the CZTS/NiO interface-defect $\leq 10^{13}$ cm^{-2} would preserve the FF. In practice, the high defects can be mitigated by ensuring smooth-surface films and interface passivation, mild annealing, and ensuring good NiO stoichiometry to avoid mid-gap states at the junction.

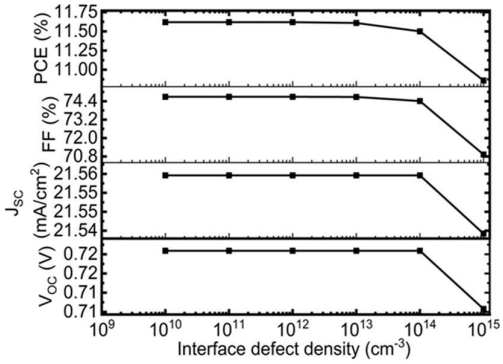

Fig. 21. (a) Variation of V_{OC}, J_{SC}, FF and PCE with defect density of the CZTS/NiO interface.

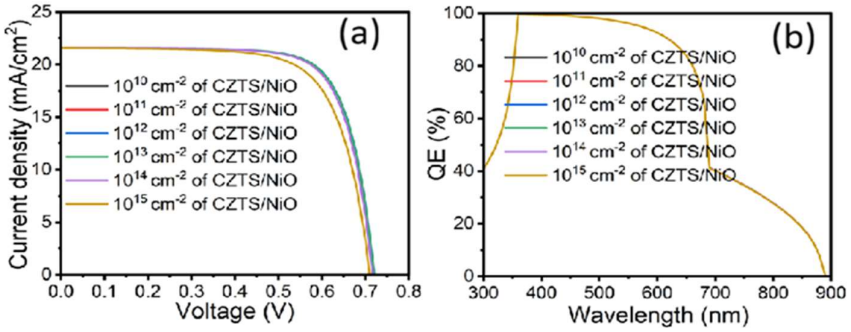

Fig. 22. (a) J-V curves with varying defect density of the CZTS/NiO interface, (b) QE plots.

E. Effect of cross-section area of electron for the absorber

Figs. 23 and 24 reveal that decreasing the electron capture cross-section in the Cs_2TiBr_6 absorber (10^{-14}–10^{-19} cm^2) yielded a small but steady performance gain that was dependent on lower SRH recombination. Reducing the electron capture cross-section increases the minority-carrier lifetime and diffusion length, slightly raising the number of collected photocarriers and hence J_{SC} (21.55–21.58 mA/cm^{-2}). This reduced the leakage current under forward bias, therefore improving the FF reasonably (74.68–75.73%). The V_{OC} remains constant (0.72 V) because the lifetime is not large enough to cause an appreciable increase in V_{OC}, which translates to a modest PCE increase (11.61–11.81%). A reduction in electron capture cross-section can be achieved in practice by passivating electron-active defects in Cs_2TiBr_6 through suitable stoichiometry and mild annealing. The steady value of J_{SC} (21.60 mA/cm^2) is supported by the overlapping QE curves (see Fig. 24b), indicating negligible variation in light absorption, carrier generation, and extraction with increasing electron capture cross-section.

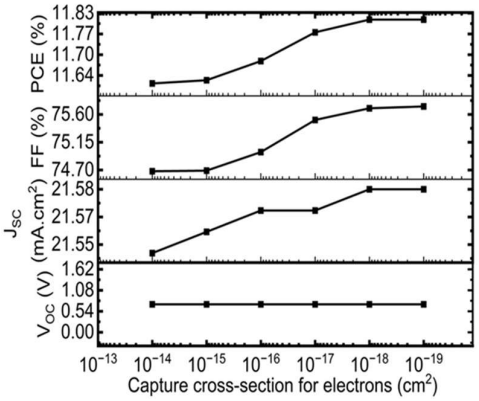

Fig. 23. (a) Variation of V_{OC}, J_{SC}, FF, and PCE with capture cross-section of electrons in the absorber layer.

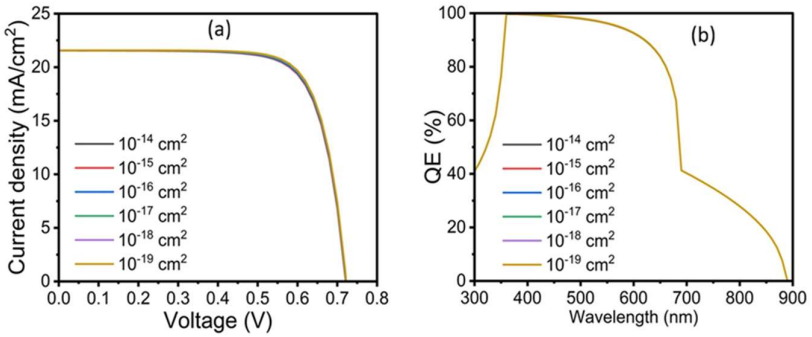

Fig. 24. (a) J-V curves with varying capture cross-section of electrons in the absorber layer, (b) QE plots.

F. Effect of operating temperature on the PSC

Figs. 25 and 26 display a gradual degradation in device performance as the operating temperature moves from 300 – 500 K. The PCE declined significantly (11.62–5.54%) because both V_{OC} and FF decreased appreciably, while J_{SC} dropped negligibly (21.56–21.52 mA/cm^2). The decline in V_{OC} (0.72–0.44 V) results from the temperature-induced increase in intrinsic carrier concentration and bandgap narrowing of the absorber, which collectively raise the dark saturation current J_0. The FF decreased (74.69–58.88%) as higher recombination increased the ideality factor and as series resistance increased. Meanwhile, J_{SC} remained nearly the same (21.52–21.56 mA/cm^2) because a slight improvement in light absorption and carrier generation near the band edge outweighed the resistive losses. The nearly steady J_{SC} could be attributed to the equivalent QE results, which indicate that light absorption and carrier generation remained constant over the tested range of operating temperature.

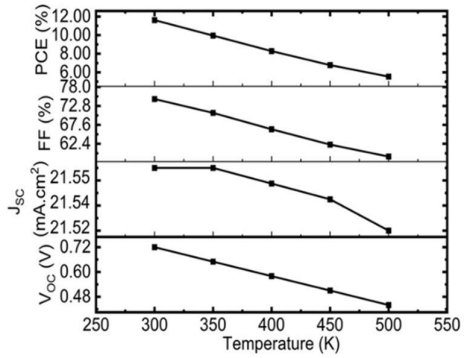

Fig. 25. (a) Variation of V_{OC}, J_{SC}, FF, and PCE with temperature.

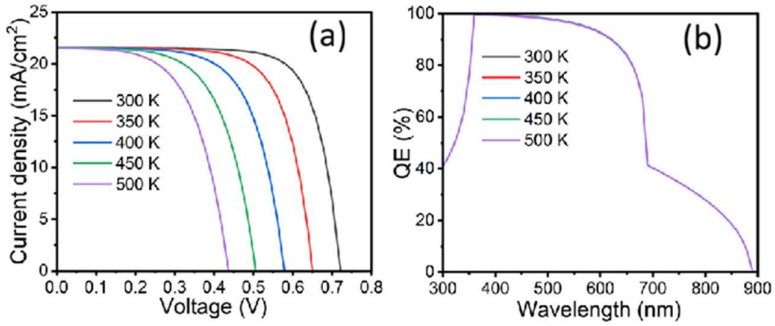

Fig. 26. (a) J-V curves with varying operating temperature, (b) QE plots.

G. *PV performance of the optimized solar cell*

The optimal parameters obtained during the prototype device simulations are thickness, bulk defect density, and electron capture cross-section of 0.5 µm, 1×10^{14} cm^{-3}, and 1×10^{-19} cm^2, respectively, for the Cs_2TiBr_6 absorber layer. The optimal thicknesses of CeO_x, CZTS, and NiO are 0.1, 1.0, and 0.2 µm, respectively. All interfaces (CeO_x/Cs_2TiBr_6, Cs_2TiBr_6/CZTS, and CZTS/NiO) have the same value of defect density (1×10^{10} cm^{-2}). Meanwhile, optimal bulk defect density of the Cs_2TiBr_6, CZTS, and NiO layers were found to be the same (1×10^{14} cm^{-3}).

The optimized device (FTO/CeO_x/Cs_2TiBr_6/CZTS/NiO) exhibited enhanced performance with a V_{OC} of 1.07 V, J_{SC} of 31.57 mA/cm^2 (see Fig. 27a), FF of 82.44%, and PCE of 27.78%. This enhanced PV performance could be traced to the moderate parameters used in the optimized design: (i) The low-defect absorber (10^{12} cm^{-3}) with an ultra-small electron capture cross-section (10^{-19} cm^2) drastically suppressed SRH recombination, prolonged the carrier lifetime and diffusion length. (ii) The absorber's initial thickness of 0.5 µm was enough to harvest most photons above the bandgap to avoid long transport paths that would reduce FF. (iii) The lower interface-defect value (10^{10} cm^{-2}) for the various interfaces

helped to minimize interfacial recombination to increase V_{OC} towards achieving high FF. (iv) The low bandgap HTL (CZTS, E_g = 1.4 eV) played the major role of photon absorption by extending the absorption to longer wavelength (near-infrared), and boosting the QE to 100% (see Fig. 27b) throughout the visible region (380-740 nm). (v) The back interface (CZTS/NiO) promoted strong hole selectivity and robust electron blocking for efficient photocarriers extracted.

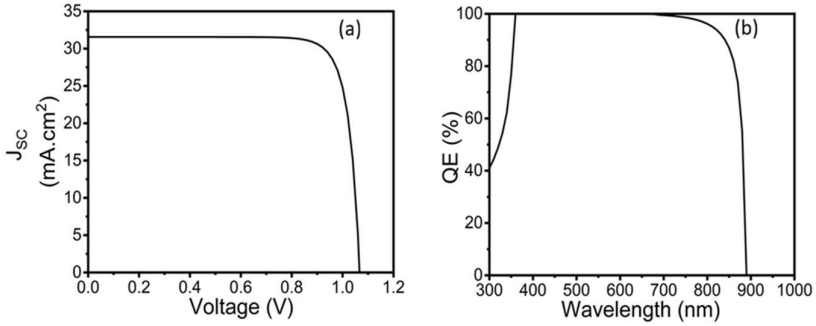

Fig. 27. (a) J-V curve of the optimized CZTS/NiO double HTL-based cell, (b) QE plot.

H. *PV performance of the optimized ETL-free PSC*

The ETL-free architectures are promising designs for perovskite PV because they offer simpler configurations, low cost, and convenience for versatile optoelectronics [16, 17, 20]. In this section, the ETL-free Cs_2TiBr_6 -based PSC (FTO/Cs_2TiBr_6/CZTS/NiO/Au) is simulated for the first time. The result of this ETL-free configuration is used to assess its viability as compared with the conventional ETL-based design (FTO/CeO_x/Cs_2TiBr_6/CZTS/NiO/Au).

Table V and Fig. 28 show that the optimized ETL-free configuration exhibited the same performance metrics as the traditional ETL-based structure, demonstrating that efficient carrier selectivity and extraction can be preserved even without a dedicated ETL. The ETL-free device behaved as a conventional ETL-based heterojunction in which the heavily absorbed Cs_2TiBr_6 formed a strong built-in electric field with the CZTS HTL, thereby promoting rapid separation of photogenerated carriers and suppressing interfacial carrier accumulation. The small conduction-band mismatch between FTO (with a work function of 4.4 eV) and Cs_2TiBr_6 (4.47 eV) introduced a modest electron extraction barrier, while the large valence-band offset effectively blocked holes from reaching the FTO contact, yielding intrinsic electron selectivity at the FTO contact. Consequently, removal of CeO_x did not introduce substantial additional leakage or extraction losses.

Table V. Comparison between the ETL-based and ETL-free optimized PSCs.

Solar cell structure	Cell type	V_{OC} (V)	J_{SC} (mA/cm^2)	FF (%)	PCE (%)
FTO/CeO_x/Cs_2TiBr_6/CZTS/NiO/Au	ETL-based	1.07	31.57	82.44	27.78
FTO/Cs_2TiBr_6/CZTS/NiO/Au	ETL-free	1.07	31.57	82.43	27.78

The high V_{OC} could be attributed to the strong suppression of non-radiative recombination in both the bulk and at interfaces. In the optimized device, the reduced bulk defect densities (10^{14} cm^{-3}) and the minimized interface defect density (10^{10} cm^{-2}) substantially lowered SRH recombination to decrease the dark saturation current (J_0), (see (4)), and increase the quasi-Fermi level splitting under illumination. This effect was reinforced by the reduced electron capture cross-section area (10^{-19} cm^2) adopted for the absorber during optimization, which directly reduced trap-assisted carrier capture rates and further suppressed recombination losses. The improved J_{SC} demonstrates nearly perfect efficiency in photogeneration-to-collection, facilitated by a diminished recombination profile and effective drift-assisted transport throughout the depletion region at the Cs_2TiBr_6/CZTS interface. The large optimized CZTS thickness (1.0 µm) additionally supported strong absorption and carrier generation at longer wavelengths, while the back-contact region (CZTS/NiO/Au) facilitated hole extraction and reduced carrier pile-up at the rear interface. Finally, the large FF indicates minimal resistive and recombination-induced curvature in the J-V characteristics, consistent with improved junction quality, reduced interfacial recombination, and sufficiently high carrier mobilities to avoid transport-limited extraction. The results obtained from the ETL-free design imply that the presence of a sufficiently selective and low-defect FTO/Cs_2TiBr_6 interface rendered the CeO_x ETL functionally redundant, enabling the ETL-free architecture to achieve a performance comparable to the ETL-assisted counterparts while potentially simplifying fabrication and mitigating transport-layer-induced parasitic losses.

$$V_{OC} = \frac{nkT}{q}\ln\left(\frac{J_{ph}}{J_0}+1\right) \quad (4)$$

where J_{ph} is the photogenerated current, J_0 the dark saturation current, n the ideality factor, q is electron charge, k is Boltzmann constant, and T is temperature [27].

The essentially equivalent PV metrics observed from the ETL-based and ETL-free designs are consistent with experimental reports on PSCs [19, 20]. Reference [19] obtained a common PCE of 13.5% from a PSC with and without introducing ZnO ETL. Similarly, [20] recorded a common PCE of 19.52%, a PSC with and without employing an ETL. Other experimental works report PCEs of 20.10% [18], 22.0% [16], 20.0% [17], and 13.60% [21], suggesting that the ETL-free approach is promising for higher efficiencies under proper engineering strategies.

Similar to the ETHL-assisted cell, the ETL-free device exhibited a QE of 100% in the wavelength range of 380-740 nm (see Fig. 28b), and then decreased sharply toward longer wavelengths (850-900 nm). The decline in QE in the long-wavelength region was mainly controlled by the absorption edge of the absorber layer. The reduced QE at shorter wavelengths (480 nm) could be traced to front-side optical losses (e.g., absorption/reflection in FTO and CeO_x) and/or stronger surface recombination of carriers generated very close to the front contact.

The high and broadband QE directly supports the large J_{SC} (see Fig. 28a), according to (5), where Φ incident photon flux, λ is wavelength, and q is the elementary charge [28].

$$J_{SC} = q\int_{\lambda_{min}}^{\lambda_{max}} \Phi(\lambda)\, QE(\lambda) d\lambda \quad (5)$$

The overlap of ETL-free and ETL-based QE curves also supported why both devices exhibited essentially the same J_{SC}. It should be noted that removing the ETL did not reduce wavelength-dependent collection of the device.

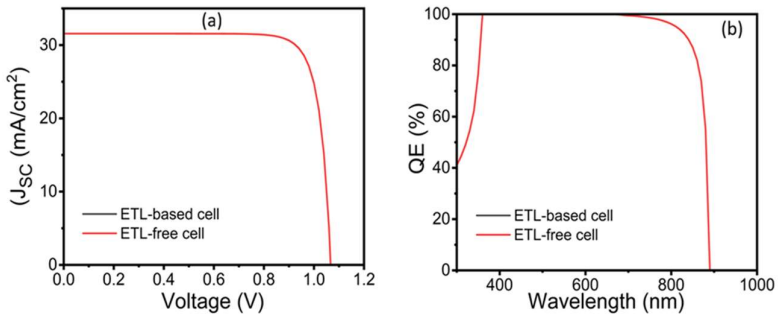

Fig. 28. (a) J-V curves of the optimized ETL-based and ETL-free cells, (b) QE plots.

Table VI compares the PV performances of the present devices with other Cs_2TiBr_6-based and ETL-free PSCs. It is observed that the present solar cells (both the ETL-assisted and the ETL-free designs) exhibited a common superior PCE value of 27.78% due to the excellent band alignment between CZTS and NiO. Reiterating, the back interface (CZTS/NiO) enhanced hole selectivity and straightened electron blocking to ensure more efficient photocarrier extraction. Interestingly, the ETL-free Cs_2TiBr_6-based cell demonstrated a significantly higher PCE (27.78%) compared to all Cs_2TiBr_6-based cells utilizing ETL (Table VI).

Table VI. Comparison of the performance metrics of experimental and simulated Cs_2TiBr_6-based perovskite solar cells

Perovskite solar cell	Nature of hole transport	Preparation method	PCE (%), FF (%), J_{sc} (mA/cm^2), V_{oc} (V)	Reference
FTO/CeO_x/Cs_2TiBr_6/CZTS/NiO/Au	HTL-based	SCAPS-1D	27.78, 82.44, 31.57, 1.07	This work
FTO/Cs_2TiBr_6/CZTS/NiO/Au	ETL-free	SCAPS-1D	27.78, 82.43, 31.57, 1.07	This work
FTO/CeO_x/Cs_2TiBr_6/CZTS/P_3HT/Au	HTL-based	SCAPS-1D	22.61, 80.35, 27.08, 1.04	[8]
FTO/TiO_2/Co_{60}/Cs_2TiBr_6/P_3HT/Au	HTL-based	Experiment	3.28, 56.4, 5.69, 1.02	[7]
FTO/TiO_2 (compact + mesoporous)/Cs_2TiBr_6/Au	HTL-free	Experiment	2.34, NA, NA, 0.89	[6]
Pt/$CuSbS_2$/ Cs_2TiBr_6/ZnO/FTO	HTL-free	SCAPS-1D	26.96, 81.36, 31.63, 1.05	[10]
FTO/SnO_2/Cs_2TiBr_6/CBTS/Au	HTL-based	SCAPS-1D	24.24, 88.9, 20.76, 1.31	[9]
Au /TiO_2/Cs_2TiBr_6/CuI/Au	HTL-based	SCAPS-1D	21.17, 81.42, 32.93, 0.79	[12]
ITO/LBSO/Cs_2TiBr_6/CNTS/Au	HTL-based	SCAPS-1D	24.82, 82.94, 26.63, 1.12	[5]
FTO/SnO_2/Cs_2TiBr_6/MoO_x/Au	HTL-based	SCAPS-1D	20.11, 82.17, 16.34, 1.45	[13]
FTO/TiO_2/Cs_2TiBr_6/MoO_3/Au	HTL-based	SCAPS-1D	15.02	[29]
FTO/CdS/Cs_2TiBr_6/Cu_2SbS_2/Au	HTL-based	SCAPS-1D	23.77, 84.76, 24.39, 1.15	[11]
Au /P_3HT/$CuSbS_2$/Cs_2TiBr_6/TiO_2/FTO	HTL-based	SCAPS-1D	21.30, 79.9, 26.20, 1.02	[30]
ITO/$MAPbI_3$/Spiro-OMeTAD or P_3HT)/Ag	ETL-free	Experiment	13.50, NA	[19]
ITO/CsFAMA /Spiro-OMeTAD/Au	ETL-free	Experiment	19.52, 77.70, 24.25, 1.04	[20]
FTO(TMAH-treated)/$FA_{0.75}MA_{0.25}PbI_{2.5}Br_{0.5}$/Spiro-OMeTAD/Au	ETL-free	Experiment	20.10, 73.80, 23.10, 1.17	[18]
FTO/$FAPbI_3$/Spiro-OMeTAD/Au	ETL-free	Experiment	22.0, NA	[16]
FTO/(low-dimensional perovskite interlayer)/3D perovskite ($FAPbI_3$-based)/Spiro-OMeTAD/Au	ETL-free	Experiment	13.6, NA	[21]

IV. Conclusion

This work reports the PV performances of the conventional ETL-assisted cell (FTO/CeO_x/Cs_2TiBr_6/CZTS/NiO/Au) and the rarely exploited ETL-free Cs_2TiBr_6-based PSC design (FTO/Cs_2TiBr_6/CZTS/NiO/Au). The addition of a CZTS/NiO bilayer significantly improved the alignment of the bands at the interface, boosted hole transport, and minimized charge recombination. This enhancement improved the QE in the longer wavelength (700 – 880 nm) and boosted the PCE of the prototype device to 11.62%. Further optimization of the absorber bulk defect density and electron capture cross-section area, bulk defect density of CZTS and CeO_x, thickness of CZTS, along with careful control of interfacial defects, resulted in an enhancement of the PCE to 27.78% for the optimized ETL-assisted device. Interestingly, the ETL-free counterpart exhibited essentially the same value of PCE (27.78%), suggesting that the CeO_x ETL is dispensable. These findings advance the comprehension of charge transport engineering in ETL-free PSCs and bolster the creation of structurally simplified and economically viable PV devices for next-generation energy systems.

Acknowledgment

The authors gratefully acknowledge the support of the UKRI Ayrton Challenge Fund (UKRI319), REACH-PSM: Resilient Renewable Energy Access Through Community-Driven Holistic Development in Perovskite Solar Module Manufacturing.

Competing interests

The authors declare that they have no known competing financial interests or personal relationships that could have influenced the work reported in this paper.

Funding

This work was supported by the UKRI Ayrton Challenge Fund (UKRI319), REACH-PSM: Resilient Renewable Energy Access Through Community-Driven Holistic Development in Perovskite Solar Module Manufacturing.

Data Availability

The data supporting the findings of this study are available from the corresponding author upon reasonable request.

Reference

[1] E. Danladi, W. Mutah, P. R. Jubu, K. A. Ogunmoye, Z. L. Abubakar, D. A. Bala, N. N. Tasie, A. Idris, F. Aungwa, M. I. Amanyi, E. Akpogum, N. I. Noah, F.: "Photovoltaic performance of $CsPbBr_3$-based perovskite solar cell with TiO_2 and quaternary chalcogenide Cu_2FeSnS_4 as charge transport channels: Unlocking >26% efficiency via SCAPS-1D investigation". *Next Energy*. vol. 9, pp. 1–16. 2025.

[2] O. S. Obaseki, M. D. J. Ooi, P. R. Jubu, F. K. Yam: "Structural, optical and transient photoelectrochemical characteristics of facile one-step fabricated ZnO/TiO_2 composite electrode". *Physica Scripta*. vol. 100, no. 1, 085941. 2025. Doi: 10.1088/1402-4896/adf267.

[3] P. R. Jubu, M. K. Omar, M. Z. Pakhuruddin: "High-efficiency p-InGaN/n-InGaN single homojunction solar cell derived by numerical simulation". *Physica Scripta*. vol. 100, pp. 1–22. 2025. Doi: 10.1088/1402-4896/ade74b.

[4] P. R. Jubu, Z. S. Mbalaha, E. V. Tikyaa, O. S. Obaseki, K. O. Ighodalo, O. Adedokun, A. Nathan-Abutu, M. B. Ochang, Y. Yusof, M. Z. Pakhuruddin: "High-efficiency hole transport layer-free perovskite solar cells utilizing TiO_2, ZnO and bilayer TiO_2/ZnO electron transport layers: A simulation approach". *Next Mat.,* vol. 9, pp. 1–17. 2025. Doi: 10.1016/j.nxmate.2025.101166.

[5] M. K. Hossain, S. Islam, M. N. Sakib, M. S. Uddin, G. F. I. Toki, M. H. K. Rubel, J. Nasrin, S. H. Shahatha, M. R. Mohammad: "Exploring the optoelectronic and photovoltaic characteristics of lead-free Cs_2TiBr double perovskite solar cells: A DFT and SCAPS-1D investigation". *Adv. Elect. Mat.,* vol. 11, 2400348. 2025. Doi: 10.1002/aelm.202400348.

[6] R. Sen, M. Yadav: "Efficient design and fabrication of Cs_2TiBr_6-based HTL-free solar cells". *Journal of Elect. Mat.,* vol. 53, pp. 1975–1981. 2024. Doi: 10.1007/s11664-024-10929-w.

[7] M. Chen, A. D. Carl, Y. Zong, R. L. Grimm, J. Gu, X.-C. Zeng, N. P. Padture: "Cesium titanium (IV) bromide thin films based stable lead-free perovskite solar cells". *Joule*, vol. 2, pp. 558–570. 2018. Doi: 10.1016/j.joule.2018.01.009.

[8] W. Lin, X. Chen, Z. Ji, W. Gao, N. Zhao, M. Li, D. Zhang, Y. Ling, J. Wu, K. Huang, J. Yu: "Optimization of Cs_2TiBr_6-based perovskite solar cells with double hole transport layer by SCAPS-1D simulation". *Mat. Today Comm.* vol. 46, 112841. 2025. Doi: 10.1016/j.mtcomm.2025.112841.

[9] S. Gupta, J. Kaur, R. Basu, A. K. Sharma, R. Pandey, J. Madan: "Lead-free Cs_2TiBr_6 perovskite solar cells achieving high power conversion efficiency through device simulation". *Micro & Nanostruct.,* vol. 196, 207991. 2024. Doi: 10.1016/j.micrna.2024.207991.

[10] H. Karmaker, A. Siddique, B. K. Das: "Numerical investigation of lead-free Cs_2TiBr_6-based perovskite solar cell with optimal selection of electron and hole transport layer through SCAPS-1D simulation". *Results in Optics*. vol. 13, 100571. 2023. Doi: 10.1016/j.rio.2023.100571.

[11] P. A. M. Mercy, K. S. J. Wilson: "Development of environmentally friendly high-performance Cs_2 $TiBr_6$-based perovskite solar cell using numerical

simulation". *App. Surf. Sci. Adv.,* vol. 15, 100394. 2023. Doi: 10.1016/j.apsadv.2023.100394.

[12] S. S. Urmi, M. A. K. Khan, T. T. Ferdous, D. Adinehloo, V. Perebeinos, M. A. Alim: "Cs_2TiI_6 ($Cs_2TiI_xBr_{6-x}$ halide perovskite solar cell and its point defect analysis". *Nanomat.,* vol. 13, 2100. 2023. Doi: 10.3390/nano13142100.

[13] J. Kaur, A. K. Sharma, R. Basu, et al.: "Numerical simulation and performance optimization of non-toxic Cs_2TiBr_6 single-halide perovskite solar cell by introducing interfacial defect layers". *Optical & Quantum Elect.,* vol. 57, 152. 2025. Doi: 10.1007/s11082-024-08023-w.

[14] R. T. Mouchou, T. C. Jen, O. T. Laseinde, K. O. Ukoba: "Numerical simulation and optimization of p-NiO/n-TiO_2 solar cell system using SCAPS". *Mat. Today: Proc.,* vol. 38, pp. 835–841. 2021.

[15] U. Farva, J. Kim: "Temperature optimization of NiO hole transport layer prepared by atomic layer deposition". *Vacuum*. vol. 207, 111674. 2023. Doi: 10.1016/j.vacuum.2022.111674.

[16] W. Hui, X. Kang, B. Wang, D. Li, Z. Su, Y. Bao, L. Gu, B. Zhang, X. Gao, L. Song, W. Huang: "Stable Electron-Transport-Layer-Free Perovskite Solar Cells with over 22% Power Conversion Efficiency". *Nano Lett*., vol. 23, no. 6, pp. 2195–2202. 2023. Doi: 10.1021/acs.nanolett.2c04720.

[17] J. F. Liao, W. Q. Wu, Y. Jiang, J. Zhong, L. Wang, D. B. Kuang: "Understanding of carrier dynamics, heterojunction merits and device physics: towards designing efficient carrier transport layer-free perovskite solar cells". *Chem. Soc. Rev.,* vol. 49, no. 2, pp. 354–381. 2020. Doi: 10.1039/c8cs01012a

[18] C. Huang, P. Lin, N. Fu, C. Liu, B. Xu, K. Sun, D. Wang, X. Zeng, S. Ke: "Facile fabrication of highly efficient ETL-free perovskite solar cells with 20% efficiency by defect passivation and interface engineering". *Chem. Comm*. vol. 55, pp. 2777–2780. 2019. Doi: 10.1039/C9CC00312F.

[19] D. Liu, J. Yang, T. L. Kelly: "Compact layer free perovskite solar cells with 13.5% efficiency". *J.of the Amer. Chem. Soc.,* vol. 136, no. 49, pp. 17116-17122, 2014. Doi: 10.1021/ja508758k

[20] Q. Han, J. Ding, Y. Bai, T. Li, J. Y. Ma, Y. X. Chen, Y. Zhou, J. Liu, Q. Q. Ge, J. Chen, et al.: "Carrier dynamics engineering for high-performance electron-transport-layer-free perovskite photovoltaics". *Chem*. vol. 4, pp. 2405–2417. 2018. Doi: 10.1016/j.chempr.2018.08.004

[21] J. Pascual, I. Kosta, T. Ngo, A. Chuvilin, G. Cabanero, H. J. Grande, E. M. Barea, I. Mora-Seró, J. L. Delgado, R. Tena-Zaera: "Electron Transport Layer-Free Solar Cells Based on Perovskite-Fullerene Blend Films with Enhanced Performance and Stability". *Chem. Sus. Chem*., vol. 9, no. 18, pp. 2679–2685. 2016. Doi: 10.1002/cssc.201600940

[22] H. Son, B.-S. Jeong: "Optimization of the power conversion efficiency of $CsPbI_xBr_{3-x}$-based perovskite photovoltaic solar cells using ZnO and NiO_x as an inorganic charge transport layer". *App. Sci.*, vol. 12, 8987. 2022. Doi: 10.3390/app12188987.

[23] C.-H. Peng, Y.-C. Lin: "SCAPS-1D simulation of various hole transport layers' impact on $CsPbI_2Br$ perovskite solar cells under indoor low-light conditions". *Solids*. vol. 6, 31. 2025. Doi: 10.3390/solids6030031.

[24] E. Danladi, L. F. Obagboye, S. Aisida, F. I. Ezema, O. Okorie, J. Bwamba, P. A. Emmanuel, A. A. Hussaini, P. R. Jubu, A. C. Ozurumba: "20.730% highly efficient lead-free $CsSnI_3$-based perovskite solar cells with various charge transport materials: A SCAPS-1D study". *Multiscale & Multidisciplinary Modeling, Experiments & Design*. vol. 8, 114. pp. 1–21. 2025.

[25] A. Itzhak, X. He, A. Kama, S. Kumar, M. Ejgenberg, A. Kahn, D. Cahen: "NiN-passivated NiO hole-transport layer improves halide perovskite-based solar cell". *ACS App. Mat. & Interfaces*. vol. 14, pp. 47587–47594. 2022. Doi: 10.1021/acsami.2c11701.

[26] C. C. Boyd, R. Shallcross, T. Moot, R. Kerner, L. Bertoluzzi, A. Onno, S. Kavadiya, C. Chosy, E. Wolf, J. Werner, J. Raiford, C. de Paula, A. Palmstrom, Z. Yu, J. Berry, S. Bent, Z. Holman, J. Luther, E. Ratcliff, N. Armstrong, M. McGehee: "Overcoming redox reactions at perovskite–nickel oxide interfaces to boost voltages in perovskite solar cells". *Joule*. vol. 4, pp. 1759–1775. 2020. Doi: 10.1016/j.joule.2020.06.00.

[27] P. Singh, N. M. Ravindra: "Temperature dependence of solar cell performance—an analysis". *Solar Energy Mat. & Solar Cells*, vol. 101, pp. 36–45. 2012. Doi: 10.1016/j.solmat.2012.02.019

[28] M. Amir, I. Masood, M. P. Singh: "Theoretical optimization of $CH_3NH_3PbI_3$-based perovskite photovoltaic cells". *Discover Elect*., vol. 2, Article 41. 2025. Doi: 10.1007/s44291-025-00080-z

[29] S. Ahmed, S. M. Mominuzzaman: "Transport layer material and thickness optimization of Cs_2TiBr_6-based solar cell". *Proc. of the 2022 12th Inter. Conf. on Elect. & Comp. Eng. (ICECE), Dhaka, Bangladesh*. pp. 280–283. 2022. Doi: 10.1109/ICECE57408.2022.10088472.

[30] N. El Aallaoui, B. Oukarfi, M. Zazoui: "Numerical study of inorganic Cs_2TiBr_6 solar cells with a double hole transport layer". *Mat. Today: Proc.,* vol. 66, pp. 122–124. 2022. Doi: 10.1016/j.matpr.2022.04.010.